Atmos. Chem. Phys. Discuss., 12, 12935–12986, 2012
www.atmos-chem-phys-discuss.net/12/12935/2012/
doi:10.5194/acpd-12-12935-2012

Atmospheric Chemistry and Physics Discussions

Identification of mercury emissions from forest fires, lakes, regional and local sources using measurements in Milwaukee and an inverse method

B. de Foy[1], **C. Wiedinmyer**[2], **and J. J. Schauer**[3]

[1]Department of Earth and Atmospheric Sciences, Saint Louis University, MO, USA
[2]National Center of Atmospheric Research, Boulder, CO, USA
[3]Civil and Environmental Engineering, University of Wisconsin – Madison, WI, USA

Received: 19 April 2012 – Accepted: 8 May 2012 – Published: 23 May 2012

Correspondence to: B. de Foy (bdefoy@slu.edu)

Published by Copernicus Publications on behalf of the European Geosciences Union.

Abstract

Gaseous elemental mercury is a global pollutant that can lead to serious health concerns via deposition to the biosphere and bio-accumulation in the food chain. Hourly measurements between June 2004 and May 2005 in an urban site (Milwaukee, WI) show elevated levels of mercury in the atmosphere with numerous short-lived peaks as well as longer-lived episodes. The measurements are analyzed with an inverse model to obtain information about mercury emissions. The model is based on high resolution meteorological simulations (WRF), hourly back-trajectories (WRF-FLEXPART) and forward grid simulations (CAMx). The hybrid formulation combining back-trajectories and grid simulations is used to identify potential source regions as well as the impacts of forest fires and lake surface emissions. Uncertainty bounds are estimated using a bootstrap method on the inversions. Comparison with the US Environmental Protection Agency's National Emission Inventory (NEI) and Toxic Release Inventory (TRI) shows that emissions from coal-fired power plants are properly characterized, but emissions from local urban sources, waste incineration and metal processing could be significantly under-estimated. Emissions from the lake surface and from forest fires were found to have significant impacts on mercury levels in Milwaukee, and to be underestimated by a factor of two or more.

1 Introduction

Elemental mercury emitted to the atmosphere has a lifetime ranging from one half to two years (Lindberg et al., 2007; Schroeder and Munthe, 1998) making it a global pollutant. There is extensive cycling between different stocks of mercury (atmosphere, oceans, lithosphere) which further adds to the timescale and complexity of mercury concentrations in the atmosphere (Selin, 2009). Mercury reacts to form methylmercury which is highly toxic and bioaccumulates in the food chain leading to global health concerns (Mergler et al., 2007).

Before 1970, the main anthropogenic sources were thought to be chloralkali plants, but dominant sources now are coal-fired power plants, waste incineration and metal processing (Schroeder and Munthe, 1998). While some point sources are well characterized with uncertainties within 30 % for power plants for example, sources such as waste incineration and various industrial processes have uncertainties of a factor of five or more (Lindberg et al., 2007). Pirrone et al. (2010) estimate current global natural sources to be 5200 t yr^{-1} and anthropogenic emissions to be 2300 t yr^{-1}. Half of the naturally emitted mercury is from the oceans, 13 % from forest fires and most of the balance from vegetation.

Streets et al. (2011) estimate the trend in emissions since 1850, showing a large peak before WWI followed by a decrease during the depression and steady growth over the last 50 yr. Atmospheric concentrations are impacted by both fresh emissions of mercury and the re-emissions of deposited mercury from terrestrial and aquatic surfaces. Although global emissions of mercury are believed to be increasing, the global average atmospheric concentration of mercury has decreased since the mid-1990s (Slemr et al., 2011). The cause of the discrepancy is unknown. One hypothesis relevant to this study is that there have been significant shifts in the re-emissions of mercury due to climate change, ocean acidification, and excess input of nutrients to terrestrial and aquatic ecosystems (Slemr et al., 2011). As regulatory controls on mercury emissions impact fresh mercury emissions and as re-emissions rates are potentially changing, there is an increased need to develop tools to quantify the emissions of mercury from air pollution sources and to quantify and track re-emissions of legacy mercury in the environment.

Emissions modeling is required to simulate natural sources of mercury, which, as noted above, are thought to account for approximately two thirds of total emissions. Lin et al. (2005) developed an emissions processor using a meteorological model to estimate continental US vegetation emissions between 28 and 127 t yr^{-1} and corresponding impacts of up to 0.2 ng m^{-3} on average gaseous elemental mercury concentrations. Bash et al. (2004) developed a surface emission model for vegetation, soils and water sources yielding flux estimates in the range of 1.5 to 4.5 ng m^{-2} h^{-1} for the three source types, in agreement with previously published estimates. However, estimates using measurements from a relaxed eddy accumulation system yielded considerably higher estimates (22 ± 33 ng m^{-2} h^{-1}) above a forest canopy (Bash and Miller, 2008). Further developing the emissions model, Bash (2010) estimate the extensive recycling of mercury that takes place between the atmosphere, terrestrial and surface water stocks. Similar emissions estimates were found by Gbor et al. (2006), who show that including natural emissions improves model performance for total gaseous mercury. Using these estimates, Gbor et al. (2007) find that their domain, which includes the Eastern US and Southeastern Canada, is a net source of mercury to the atmosphere.

Comparison of measurements in coastal and rural sites found impacts of surface water emissions of mercury on atmospheric concentrations (Engle et al., 2010). Ocean emissions were also found to impact mercury levels in New Hampshire (Sigler et al., 2009). A modeling study found that although globally the ocean is a sink of mercury, the North Atlantic is a net source with 40 % of the emissions coming from subsurface water. These are potentially due to historical anthropogenic sources (Soerensen et al., 2010).

Chemical grid modeling of mercury has been developed mainly to estimate deposition rates and is subject to a combination of large uncertainties in emissions as well as in chemical reactions (Lin and Tao, 2003; Roustan and Bocquet, 2006; Seigneur et al., 2004; Bullock et al., 2008). Yarwood et al. (2003) used grid modeling to evaluate mercury deposition in Wisconsin and found that there was a significant need to improve model boundary conditions and the treatment of wet deposition. A further study by Seigneur (2007) found that anthropogenic North American sources likely contributed between 15 and 40 % of mercury deposition in Wisconsin, with less than 10 % contribution from US coal-fired power plants.

Sprovieri et al. (2010) review worldwide measurements of atmospheric mercury and note that there are significant unknowns in the spatial distribution of mercury deposition in relation to sources. For example, there can be low values of deposition close to large power plants in Pennsylvania and Ohio, and high values in Florida. Furthermore, values in urban locations can be a factor of two or greater than at rural sites. Murray and Holmes (2004) had already noted differences by up to a factor of two in different emissions inventories for the Great Lakes and identified that some industrial sources have particularly uncertain emissions. Nevertheless, Cohen et al. (2004) found that estimated deposition rates to the Great Lakes were consistent with measurements. Using a model for particle trajectories, they show that sources up to 2000 km away can have significant impacts and that coal combustion is the largest contributor although sources such as incineration and metal processing are significant too.

There have been several measurement studies in Wisconsin aimed at identifying sources of mercury. Manolopoulos et al. (2007a) made year long measurements at a rural site and found significant impacts from a local coal-fired power plant on reactive gaseous mercury, but not elemental mercury. They recommend the use of receptor-based monitoring to account for small-scale sources and processes that cannot be represented in large-scale grid models. Kolker et al. (2010) perform a separate study with three rural measurement sites. They find that the site closest to the coal-fired power plant does not always experience the highest mercury levels and suggest three possible reasons: the presence of a chlor-alkali facility, the plume height, and/or the formation of reactive gaseous mercury in the plume. They do find that elevated levels are due to wind transport from the south, but cannot differentiate between local sources or the more distant Chicago area which is in the same direction. Rutter et al. (2008) compare measurements from the rural site reported in Manolopoulos et al. (2007a) and from an urban site in Milwaukee. They report on a significant urban excess in elemental gaseous mercury and suggest that point sources could account for a third of the gaseous elemental mercury in Milwaukee. Further analysis by Engle et al. (2010) includes a comparison of this data with other rural, urban and coastal sites in the US, and further reinforce the suggestion that mercury in Milwaukee is significantly impacted by local point sources.

Measurements studies in other urban locations in the US and Canada reinforce the finding that improvements in mercury inventories are needed, especially because of missing urban point sources. Manolopoulos et al. (2007b) find that in East St. Louis mercury concentrations were more likely influenced by very local sources (within 5 km) than by the power plants within a 60 km radius. Liu et al. (2010) find that Detroit has an urban excess in mercury concentrations similar to that reported for Milwaukee. Measurements in upstate New York were combined with back-trajectories to identify large point sources in the Northeast as well as in Southern Canada (Han et al., 2005) with further possible impacts from Taconite mining around the Great Lakes. Further measurements from the same location identified impacts that were more from industrial areas in the Midwest than the previous study, but also identified the Atlantic Ocean as a possibly significant source (Han et al., 2007). In Rochester, Huang et al. (2010) found impacts from a local coal-fired power plant as well as signatures suggestive of melting snow and local mobile sources.

In Toronto, Cheng et al. (2009) report that the major contributors to mercury levels are industrial sources rather than power plants. Modeling using particle back-trajectories reinforced the importance of local sources but underscored the need to consider natural sources as well (Wen et al., 2011). In agreement with Manolopoulos et al. (2007a), they showed that local trajectory simulations can capture the impacts of local sources better than grid models. At a remote rural site in Western Ontario, Cheng et al. (2012) used back-trajectories to identify distant sources, but also found that mixing and overlap of sources reduces the ability of the model to identify specific source factors.

This study combines the urban measurements from Milwaukee (Rutter et al., 2008) with meteorological analysis and back-trajectory simulations to identify sources responsible for the gaseous elemental mercury concentrations. We intentionally restrict the study to the transport of gaseous elemental mercury and consequently do not consider chemical transformation and deposition. We develop a hybrid inverse model to evaluate the varied sources of mercury: local, regional and distant sources, forest fires and lake surface emissions.

2 Methods

2.1 Measurements

Ambient mercury measurements were made at an urban site located north of downtown Milwaukee at 2114° E. Kenwood Blvd, Milwaukee, WI, USA (43°06′29″ N, 87°53′02″ W). The location is 0.5 to 1 mile from Lake Michigan. Measurements were made from 28 June 2004 to 11 May 2005 (inclusive). A real time in situ ambient mercury analyzer was used from Tekran, Inc., to measure gaseous elemental mercury (GEM), reactive gaseous mercury (RGM) and particulate mercury (PHg). In this study we focus on the GEM measurements. Ambient air was pumped into the instrument at a rate of $10\,\mathrm{l}^{-1}$min for 1 h followed by 1 h for analysis of RGM and PHg. GEM was collected onto gold granules over 5 min periods during the hour that RGM and PHg were collected. It was then thermally extracted and measured using Cold Vapor Atomic Fluorescence Spectroscopy (CVAFS). The measurement are described in greater detail in Rutter et al. (2008) and the references therein.

For the meteorological analysis, we use Integrated Surface Hourly Data from the National Climatic Data Center which has hourly wind and temperature observations. The nearest site is at General Mitchell International Airport 10 miles south of the measurement site.

2.2 Meteorological simulations

Mesoscale meteorological simulations were performed using the Weather Research and Forecasting Model (WRF) version 3.3.1 (Skamarock et al., 2005). The boundary and initial conditions were obtained from the North American Regional Reanalysis (Mesinger et al., 2006) which has a horizontal resolution of 32 km. WRF was run with two-way nesting on 3 domains of 27, 9 and 3 km horizontal resolution with 41 vertical levels. Figure 1 shows a map with the three domains. The model set-up is identical to the one described in de Foy et al. (2012).

We used the Yonsei University (YSU) boundary layer scheme (Hong et al., 2006), the Kain-Fritsch convective parameterization (Kain, 2004), the NOAH land surface scheme, the WSM 3-class simple ice microphysics scheme, the Goddard shortwave scheme and the RRTM longwave scheme. 69 individual simulations were performed each lasting 162 h: the first 42 h were considered spin-up time, and the remaining 5 days were used for analysis.

2.3 Lagrangian simulations

Stochastic particle trajectories were calculated with FLEXPART (Stohl et al., 2005) using WRF-FLEXPART (Fast and Easter, 2006; Doran et al., 2008). Back-trajectories were calculated for every hour of the campaign by releasing 1000 particles throughout the hour from a randomized height between 0 and 50 m above the ground. Particle locations were calculated for 6 days and were saved every hour for analysis. Vertical diffusion coefficients were calculated based on the WRF mixing heights and surface friction velocity. Sub-grid scale terrain effects were turned off and a reflection boundary condition was used at the surface to eliminate all deposition effects.

Residence Time Analysis (RTA, Ashbaugh et al., 1985) was obtained by counting all particle positions every hour on a grid. This yields a gridded field representing the time that the air mass has spent in each cell before arriving at the receptor site. The units of this field are in particle · hours.

The RTA can be used for a Concentration Field Analysis (CFA, Seibert et al., 1994) to identify potential source regions using concentration measurements at a receptor site, see also (de Foy et al., 2009, 2007). Results will be presented using the GEM concentrations and a grid with 45 km resolution that covers most of WRF domain 1.

For the inverse method, the choice of grid has a much greater impact on the results. It is important to choose a grid that has a resolution similar to the resolution capability of the models. We therefore choose a polar grid shown in Fig. 1 with 18 cells in the circumferential direction and 20 in the radial direction. It has a 20° resolution and an initial radial distance of 10 km increasing linearly by 15 % reaching a maximum radial grid thickness of 142 km at a distance of 1024 km.

2.4 Lake surface emissions

Emissions of mercury from the lake surfaces were calculated using the method described in Ci et al. (2011a,b). This is based on a two-layer gas exchange model described by Eq. (1):

$$F = K_w(C_w - C_a/H') \quad (1)$$

F is the GEM flux in $\mathrm{ng\,m^{-2}\,h^{-1}}$. K_w is the water mass transfer coefficient given by Wanninkhof (1992), which is a function of the surface wind speed and the Schmidt number. The Schmidt number is defined as the kinematic viscosity divided by the aqueous diffusion coefficient of elemental mercury. Kuss et al. (2009) determined the diffusion coefficient and found that it is nearly identical to that for carbon dioxide for the temperature range of interest. The parameterizations for the latter can therefore be used for the former in the present case. H' is the Henry's Law constant and is based on the lake temperature. C_w is the concentration of Dissolved Gaseous Mercury (DGM) in the surface waters, measured in $\mathrm{pg\,l^{-1}}$, and C_a is the concentration of atmospheric GEM measured in $\mathrm{ng\,m^{-3}}$. Overall, the emissions fluxes from Ci et al. (2011a) are higher but follow a similar pattern as those estimated from the parameterization of Poissant et al. (2000).

The Great Lakes are super-saturated in mercury with respect to the atmosphere such that the flux is from the water to the air (Vette et al., 2002; Poissant et al., 2000). For C_a we use a background value of $1.5\,\mathrm{ng\,m^{-3}}$, as reported by Rutter et al. (2008). For C_w, Poissant et al. (2000) report measurements made in 1998 of 50 to $130\,\mathrm{pg\,l^{-1}}$ during a transect of Lake Ontario and around $30\,\mathrm{pg\,l^{-1}}$ in the Upper St. Lawrence River. These are on the high end of measurements reported in the literature (Lai et al., 2007) which found values of $16\,\mathrm{pg\,l^{-1}}$ in Lake Ontario. For Lake Michigan, Vette et al. (2002)

found DGM concentrations around 20 pg l^{-1} during measurements in 1994. We chose to use 30 pg l^{-1} as a domain wide average in this study.

The emissions were calculated for WRF domains 1 and 2 using lake temperatures interpolated from the NARR, and hourly 10-m wind speeds from the model. WRF domain 1 covers all five of the Great Lakes and domain 2 covers Lake Michigan. Figure 2 shows the map of emissions of GEM summed over the duration of the campaign. Total emissions and average fluxes are reported for each lake in Table 1. Total emissions from the 5 lakes were 6 849 kg yr^{-1} for 318 days, and average fluxes were 2.3 ng m^{-2} h^{-1}.

Concentrations of GEM due to lake surface emissions were simulated at the receptor site using the Comprehensive Air-quality Model with eXtensions (CAMx, ENVIRON, 2011), version 5.40. This was run on WRF domains 1 and 2 (resolution 27 and 9 km) with the first 18 of the 41 vertical levels used in WRF using the O'Brien vertical diffusion coefficients (O'Brien, 1970).

During the testing of the inverse model, the estimates of the lake emissions were very robust across different time selections except for two time periods: from 28 June to 18 July, and from 1 to 11 August 2004. Pending further analysis, these two time periods were therefore removed from the time series, as can be seen if Fig. 10.

2.5 Forest fires

Emissions of mercury from open fires, including wildfires, agricultural burning and prescribed burns, were calculated using the Fire INventory from NCAR (FINN) version 1, an emission framework method described in Wiedinmyer et al. (2006) and Wiedinmyer et al. (2011). Fire counts for North America were downloaded from the US. Forest Service Remote Sensing Applications Center for 2003 through 2005 (http://activefiremaps.fs.fed.us/gisdata.php?sensor=modis&extent=north_america). These data are from the Terra and Aqua MODIS fire and thermal anomalies data provided from the official NASA MCD14ML product, Collection 5, version 1 (Giglio et al., 2003). Land cover and vegetation density was determined with the MODIS Land Cover Type product (Friedl et al., 2010) and the MODIS Vegetation Continuous Fields product (Collection 3 for 2001) (Hansen et al., 2003, 2005; Carroll et al., 2011), and fuel loadings from Hoelzemann et al. (2004) and Akagi et al. (2011). Emission factors for mercury emissions were provided by Wiedinmyer and Friedli (2007).

Figure 3 shows the sum of the emissions over the duration of the measurements. This domain covers the continental US and most of Canada, which is much larger than WRF domain 1 used above. We therefore perform a second set of meteorological simulations with a single domain of 121 by 91 cells and a resolution of 64 km. We separate the emissions into sub-domains shown in Fig. 3 and perform individual CAMx simulations for each one. In this way, we obtain time series of concentrations at the measurement site due to fires in the following geographical areas: Alaska, Northern Canada, pacific northwest, west (mainly fires in California and Southern Oregon), north central, south central, southeast and east. Fires within WRF Domain 2 are simulated separately from the rest of the east domain using the higher resolution WRF simulations above.

2.6 Inverse method

Because gaseous elemental mercury is a long-lived species, we can assume a linear relationship between an emissions vector $\boldsymbol{x}$ and the measurements $\boldsymbol{y}$ given by the sensitivity matrix $\mathbf{H}$ (Rigby et al., 2011; Brioude et al., 2011; Stohl et al., 2009; Lauvaux et al., 2008):

$$\boldsymbol{y} = \mathbf{H}\boldsymbol{x} + \text{residual} \tag{2}$$

Following Tarantola (1987) and Enting (2002), and as described in the papers above, we can write the cost function J as the sum of the cost function for the observations and for the emissions vector:

$$J = J_{\text{obs}} + J_{\text{emiss}} \tag{3}$$

$$J = (\mathbf{H}\boldsymbol{x} - \boldsymbol{y})^T \mathbf{R}_a^{-1} (\mathbf{H}\boldsymbol{x} - \boldsymbol{y}) + \boldsymbol{x}^T \mathbf{R}_b^{-1} \boldsymbol{x} \tag{4}$$

Where $\mathbf{R}_a$ is the error covariance matrix corresponding to the sensitivity matrix $\mathbf{H}$, and $\mathbf{R}_b$ is the error covariance matrix on the emissions factors in $\boldsymbol{x}$.

The sensitivity matrix $\mathbf{H}$ can be composed of multiple components, as was done in Rigby et al. (2011). In this work, we combine the sensitivities from the back-trajectories obtained using WRF-FLEXPART, the sensitivities from forward simulations using CAMx and the sensitivities due to background values:

$$\mathbf{H} = (\mathbf{H}_{\mathrm{RTA}}, \mathbf{H}_{\mathrm{CAMx}}, \mathbf{H}_{\mathrm{Bkg}}) \tag{5}$$

$$\boldsymbol{x} = (\boldsymbol{x}_{\mathrm{RTA}}, \boldsymbol{x}_{\mathrm{CAMx}}, \boldsymbol{x}_{\mathrm{Bkg}})^T \tag{6}$$

$\boldsymbol{x}_{\mathrm{RTA}}$ contains the gridded emissions parameters, and $\mathbf{H}_{\mathrm{RTA}}$ is the Residence Time Analysis from WRF-FLEXPART that contains the impacts of the emissions in a grid cell on the concentrations at the measurement site. $\boldsymbol{x}_{\mathrm{CAMx}}$ are the scaling factors on the concentrations obtained from CAMx simulations contained in $\mathbf{H}_{\mathrm{CAMx}}$. Finally, the background values are contained in $\boldsymbol{x}_{\mathrm{Bkg}}$ and $\mathbf{H}_{\mathrm{Bkg}}$. This can be limited to a single value or be expanded for a varying background in time.

If we have a priori values $\boldsymbol{x}_o$ for the emissions factors $\boldsymbol{x}$, we modify the equations to solve for adjustments to the a priori emissions factors ($\boldsymbol{x}'$) instead of solving for emissions factors directly:

$$\boldsymbol{x}' = \boldsymbol{x} - \boldsymbol{x}_o \tag{7}$$

$$\boldsymbol{y}' = \boldsymbol{y} - \mathbf{H}\boldsymbol{x}_o \tag{8}$$

In order to simplify the solution of the system, the cost function of the emissions vector (J_{emiss}) can be folded into the J_{obs} term by augmenting the sensitivity matrix $\mathbf{H}$ with diagonal terms and the observation vector $\boldsymbol{y}$ with zero values, so that we have:

$$J = (\mathbf{H}''\boldsymbol{x} - \boldsymbol{y}'')^T \mathbf{R}^{-1} (\mathbf{H}''\boldsymbol{x} - \boldsymbol{y}'') \tag{9}$$

Where $\mathbf{H}'' = (\mathbf{H}, \mathbf{D})$ and $\boldsymbol{y}'' = (\boldsymbol{y}, \boldsymbol{x}_{\mathrm{zero}})$ are the augmented versions of $\mathbf{H}$ and $\boldsymbol{y}$ (or of $\mathbf{H}'$ and $\boldsymbol{y}'$ if using a priori emissions). $\mathbf{D}$ is a diagonal matrix the size of $\boldsymbol{x}$, and $\boldsymbol{x}_{\mathrm{zero}}$ is a vector of zero values. The new error covariance matrix is given by $\mathbf{R} = (\mathbf{R}_a, \mathbf{R}_b)$.

The error covariance matrices are often taken to be diagonal matrices because of a lack of information on the off-diagonal elements (Brioude et al., 2011; Stohl et al., 2009). In this case, Eq. (9) simplifies to a linear least-squares problem, where each row i is scaled by a scaling factor $\boldsymbol{s}_i$ determined from the diagonal terms of the error covariance matrix **R**.

$$J = \|\boldsymbol{s} \cdot (\mathbf{H}''\boldsymbol{x} - \boldsymbol{y}'')\|_2 \tag{10}$$

The purpose of using this formulation is to simplify the equation to a single least-squares problem so that constraints can be applied easily to the emissions vector $\boldsymbol{x}$. Solution methods for Eq. (4) will generate negative emission values by default (Stohl et al., 2009; Brioude et al., 2011). These corrupt the solution by obtaining an excellent fit for the linear model (Eq. 2) from a combination of unphysical values. Stohl et al. (2009) solve this problem by iteration. After each solution, the error covariance terms are adjusted to force the posterior emissions closer to the a priori emissions for those points that would be negative. Brioude et al. (2011) address the problem by working with the log of the concentrations. In this work, we apply constraints to the solution of the linear least-squares problem directly to Eq. (10). In this way, the solution $\boldsymbol{x}$ can be found by straightforward application of the Matlab function lsqlin.

The vector $\boldsymbol{s}$ contains scaling terms for individual contributions from the vector $\boldsymbol{x}$. Initially, values are assumed to be homogeneous within J_{obs} and J_{emiss}, which means that in practice $\boldsymbol{s}_i$ for the observations are set to 1 and those for the emissions factors are set to a regularization parameter α (Brioude et al., 2011; Henze et al., 2009). This parameter excercises a constraint on the magnitude of the emissions factors (or on the adjustments when using a priori emissions). Because it relates the importance of the cost function of the measurements with that of the emissions factors it is not a dimensionless number. Based on testing, it was set to a value of 1×10^{-4}. After the first solution of the least-squares problem, the magnitude of the residual in Eq. (2) is used to refine estimates of $\boldsymbol{s}_i$. Observation times that have a residual larger than 3 times the standard deviation of the residual values are assigned a scaling factor of 0. This process converges on stable values of $\boldsymbol{s}$ after 2 to 4 iterations.

When obtaining the solution, one must pay close attention to the units of the system. The measurements $\boldsymbol{y}$ are in units of $\mathrm{ng\,m^{-3}}$ and the emissions $\boldsymbol{x}$ were calculated in units of $\mathrm{lb\,yr^{-1}}$ to be consistent with the EPA emissions inventories. The Residence Time Analysis matrix $\mathbf{H}$ is in units of particle·hours. This means that we need to scale the product $\mathbf{H}\boldsymbol{x}$ by a factor with units of $\mathrm{ng\,lb^{-1} \cdot yr\,h^{-1} \cdot 1\,(particle \cdot volume)^{-1}}$. For the last term on the right we use the maximum number of particles in a simulation (1000 in our case) multiplied by the volume of the grid cells in the Residence Time Analysis. The height of the cells used for counting particles to obtain the RTA matrix must be chosen to be large enough to have a sufficient number of particle counts, and small enough to provide a value that is related to the measurements which are surface concentrations. In practice, we choose a value of 1000 m which corresponds to the mixing height for the time scales corresponding to the transport distances in the polar grid used.

To obtain a posteriori confidence intervals on the results, we use the bootstrap method. Multiple instances of the model are run with a random selection, with replacement, of both the times and the emission factors. Measurement times used in the analysis are randomly selected leading to a modified measurement vector $\boldsymbol{y}$ and corresponding selection of the rows in $\mathbf{H}$. Emission factors from the particle grid ($\boldsymbol{x}_{\mathrm{RTA}}$) are also randomly selected leading to rearrangement of the columns of $\mathbf{H}_{\mathrm{RTA}}$. The CAMx time series are used with a probability of 75 % in any given simulation. In practice this is done by resetting columns of $\mathbf{H}_{\mathrm{CAMx}}$ to zero with a probability of 25 %.

3 Results

Before describing the inverse method, we present a preliminary analysis using simpler methods. Figure 4 shows the time series of elemental gaseous mercury concentrations, which was analyzed by Rutter et al. (2008). As described above, there are 3594 data points which are hourly concentrations measured on alternate hours from 28 June

2004 to 11 May 2005 (inclusive). There are a combination of features ranging from the hourly scale to the daily and weekly scale. High peaks of short duration suggest narrow plumes from point sources. These were estimated to make up one third of the GEM in Rutter et al. (2008). Longer peaks such as in the second half of November 2004 or during April 2005 suggest larger scale phenomena.

Figure 5 shows windroses corresponding to low, high and very high GEM levels. The dominant winds during concentrations in the bottom 50 % are from the northwest. For high concentrations, defined as being in the 50 % to 95 % range, the winds are predominantly from the south-southwest and from the north-northeast. The top 5 % of concentrations take place when there are winds from the northeast and from the southwest. The bars in the windroses are colored by time of day and show that the northeast winds are associated with afternoon winds whereas the southwest winds are more likely to be before sunrise.

Figure 6 shows the Residence Time Analysis and the Concentration Field Analysis for a domain covering most of WRF domain 1 for the entire time period. The RTA is in agreement with the windroses and shows that the dominant wind transport to Milwaukee is from the northwest, from the northeast over Lake Michigan and from the south-southwest through Illinois. The southeast area has the smallest contribution to airmass transport at the receptor site. The CFA shows that there are unlikely to be significant mercury sources to the northwest, in agreement with the windroses. The northeast signature in the windroses corresponds to a significant potential source region over the Great Lakes in the CFA analysis. Finally, south-southwest transport of mercury to Milwaukee corresponds to transport from industrial regions to the south. As CFA does not distinguish easily between positions along the plume path, these could be a combination of local sources south of the measurement site, more distant sources from the Chicago area or sources beyound that. Althouh the airmass does not frequently come over the Ohio River Valley, when it does it is associated with high GEM levels.

3.1 Synthetic inverse

The inverse method was tested using synthetic data corresponding to continuous emissions from a point 213 km to the northwest of the measurement site. Synthetic concentrations were simulated using CAMx as input for the inversion. Residual scaling was applied and converged on the fourth iteration, with 177 measurements excluded from the analysis (out of a total of 7657). Figure 7 shows the map of the inverse emissions, clearly showing that the model correctly identifies the source cell. The emission strength from the actual emission grid cell was underestimated by 25 %. If we include the neighboring grid cells in the emission strength, then the underestimate is reduced to 18 %. Because the model simulates emissions from cells further away, there is an overall over-estimation of the emissions by 21 %. Taking emissions from the 9 grid cells around the source, we find that 68 % of the emissions in the inversion come from the correct area.

One can see from the emissions map (Fig. 7) that the model is better at resolving the direction of the source than the distance from the source. Furthermore, the model has a tendency to overestimate distant sources. This happens if the particular grid cells happens to have a single impact that coincides with a high concentration peak at the measurement site. There are three ways of mitigating this problem in the current setup. The first is by using a polar grid with increasing cell sizes. This makes it less likely to have a chance correlation between the RTA and the concentrations. The second is to use iterative residual scaling which prevents the scheme from trying to match peaks that it cannot resolve. The third is to use the regularization parameter α which balances the cost function between the measurements and the emissions factors. By increasing this, the model will reduce the overal amount of predicted emissions.

3.2 Full inverse

The inversion algorithm was run on the actual data (3594 data points) using the polar grid consisting of 360 grid cells, the 9 CAMx concentration time series for the forest fires domains, one CAMx concentration time series for the lake surface emissions and a single value for the background. The augmented matrix $\mathbf{H}''$ contains a further 360 rows with the weighting factors in the diagonal. This leads to the solution of a linear system of equations with dimensions of 3954×371. Because the actual inversion takes of the order of one second to run on a desktop, it can be easily carried out for 100 bootstrapped simulations of 5 iterations each. The 5 iterations allow the residual scaling to converge and the 100 bootstrapped simulations provide a measure of uncertainty on the solution vector $\boldsymbol{x}$. For the simulations presented we do not use a priori emissions, instead leaving the inversion algorithm to identify source regions irrespective of previous estimates.

Figure 8 shows the inverse emissions grids in units of $\mathrm{kg\,yr^{-1}}$, using the median of the 100 bootstrapped runs. Table 3 shows the total emissions, tabulated according to the geographic region for the domains shown in Fig. 11. The table also shows the lower quartile and upper quartile values of the bootstrapped simulations which represent a measure of the variability of the results.

The largest sources are from grid cells over the Ohio River Valley to the southeast, which is an area known for its large coal-fired power plants. Overall, the model estimates emissions of $23\,000\,\mathrm{kg\,yr^{-1}}$ from the southeast domain. The southwest domain emissions are estimated to be $24\,000\,\mathrm{kg\,yr^{-1}}$ from a larger number of grid cells corresponding to emissions from a broader area. After this, the northeast domain accounts for $13\,000\,\mathrm{kg\,yr^{-1}}$ coming from upper Michigan, Eastern Canada, the US Northeast, Lake Huron and Lake Superior. The remaining domains have lower estimated emissions. To the northwest there are $6000\,\mathrm{kg\,yr^{-1}}$ from the upper Great Plains. Closer in, there are $3500\,\mathrm{kg\,yr^{-1}}$ from regional sources to the west and $6000\,\mathrm{kg\,yr^{-1}}$ from regional sources to the south, which include Chicago. The local domain counts sources within a 50 km radius of the measurement site, for a total of $1000\,\mathrm{kg\,yr^{-1}}$.

Figure 9 shows histograms of the scaling factors applied to the CAMx simulated timeseries of forest fires and lake surface emissions. Median, lower quartile and upper quartile values are shown in Table 4. The lake surface emissions have a very reliable scaling factor with a median value of 1.9 and an interquartile range of 1.7 to 2.2. This suggests that the results are robust relative to the selection of time periods and are not sensitive to the selection of grid points or forest fires timeseries included in the inversion.

The forest fires factors vary across the domains shown in Fig. 3. The most reliable result is a median factor of 3.9 (inter-quartile range 3.1 to 4.5) for fires in the east domain excluding WRF domain 2. Fires for the north central domain have consistent scaling factors of 2.6 on average (IQR 2.2 to 3.3). After these, the south central and southeast domain have scaling factors of 1.2 (IQR 0.8 to 1.6) and 1.1 (IQR 0.6 to 1.6), respectively. The scaling factor for the West domain has a large variation, ranging from 3.9 to 10.1, but with the full range extending to zero values. The rest of the domains have very low scaling factors. Northern Canada has an inter-quartile range of 0.02 to 0.17 and Alaska and the pacific northwest have zero values. Fires within WRF domain 2, close to the measurement site, also have scaling factors of 0.

Figure 10 shows the inverted time series (given by $\mathbf{H}\boldsymbol{x}$) along with the original measurements ($\boldsymbol{y}$). The median Pearson correlation coefficient (r) between the two is 0.39 for the complete time series and 0.58 when excluding the times removed by the residual scaling.

The background value determined from the model is $1.99\,\mathrm{ng\,m^{-3}}$ (IQR 1.98 to $2.01\,\mathrm{ng\,m^{-3}}$) and is very stable across model configurations. Rutter et al. (2008) measured background concentrations of $1.5\,\mathrm{ng\,m^{-3}}$ at a rural site 150 km to the west and annual average concentrations of $1.6\,\mathrm{ng\,m^{-3}}$. This suggests that the discrepancy of $0.49\,\mathrm{ng\,m^{-3}}$ can be separated into $0.1\,\mathrm{ng\,m^{-3}}$ from regional background and $0.4\,\mathrm{ng\,m^{-3}}$ due to local sources in and around Milwaukee.

The time series of the contribution from the gridded emissions, the forest fires and the lake surface emissions are shown in the bottom panel of Fig. 10. The gridded emissions are assumed to be constant throughout the year and vary at both daily and synoptic time scales depending on the prevailing wind directions. The forest fires has a clear seasonal component, as expected. The highest contribution occurs during the high

GEM event of April 2005 as well as during the smaller but more frequent events during fall 2004. The lake surface emissions are temperature dependent and therefore have a similar seasonal pattern, except that they are less influenced by individual events. Compared with the forest fires impacts, the lake surface also contributes to the April 2005 event, but it has a more continuous impact during the late summer of 2004. There are sporadic lake surface impacts at the measurement site throughout the fall, winter and spring.

3.3 Impacts of estimated source groups on average GEM concentrations

Table 5 shows the impacts of specific source groups on the average GEM concentrations at the receptor site. The results for the grid domains are aggregated from the grid cell impacts shown in Fig. 11. The table shows the median values and the inter-quartile range from the bootstrapped runs. Figure 12 shows the impacts from the inverse model for the Great Lakes, the forest fires and the gridded emissions by geographical domain. Overall, the measurements have an average concentration of 2.48 ng m^{-3} and the model inversion timeseries has an average of 2.33 ng m^{-3}, leaving an unaccounted for gap of 150 pg m^{-3}. The greatest contributions to the inverted time series are from the global background (1.5 ng m^{-3}) and from the additional local and regional background (0.49 ng m^{-3}).

This leaves contributions of 188 pg m^{-3} from the gridded emissions, 86 pg m^{-3} from the forest fires and 61 pg m^{-3} from the lake surface emissions. The impacts due to the gridded emissions, shown in Fig. 11 are the product of the estimated emissions of a grid cell times the impact of that grid cell on the measurement site, obtained from the Residence Time Analysis. The large sources from the southeast and the southwest can be seen to contribute 16 pg m^{-3} and 23 pg m^{-3}, which are low values because the air mass in Milwaukee does not often come from those directions (see Fig. 6). The middle panel of Fig. 11 shows that the regional impacts from the south are mainly due to the Chicago area with an estimated contribution of 30 pg m^{-3}. The main contributor from the gridded emissions are the local sources with impacts of 64 pg m^{-3}. These can be seen in the right panel of Fig. 11 to be close to the source as well as to the southwest of the measurement site, which is the direction of the Menomonee valley industrial corridor.

The fire contributions are mainly from the east domain, with average concentrations of 46 $\text{pg}\,\text{m}^{-3}$. Next come the southeast, south central and north central domains with contributions of approximately 10 $\text{pg}\,\text{m}^{-3}$. As noted above, the contributions from the west have a large uncertainty range, as do the ones from Northern Canada. The contributions from the the local fires, the pacific northwest and Alaska were all 0.

4 Discussion

4.1 Comparison with the toxic release inventory and national emissions inventory

The estimated gridded emissions in Fig. 8 can be compared with the US emissions from the 2004 Toxic Release Inventory (TRI) and those from the 2002 National Emissions Inventory (NEI), as shown in Fig. 13. TRI version 10 files were obtained from the US Environmental Protection Agency's website. These contain separate emission values for mercury and mercury compounds, which have been added together in the present work. The 2002 NEI Hazardous Air Pollutant inventory was obtained for point sources, using the files dated 23 January 2008 also available from the EPA's website. These contain separate values for elemental mercury, gaseous divalent mercury, particulate divalent mercury as well as two additional categories called "mercury" and "mercury and compounds". Here we use the emissions of elemental mercury as well as the total of all mercury types put together.

Total emissions are listed by domain in Table 3 for comparison with the model results. In terms of spatial distribution, the Ohio River Valley clearly stands out as it did in the model results. The two different inventories are in agreement on these sources with magnitudes within a factor of 2 of each other. The model estimated sources were in the

Title Page
Abstract Introduction
Conclusions References
Tables Figures
◀I ▶I
◀ ▶
Back Close
Full Screen / Esc
Printer-friendly Version
Interactive Discussion

range (IQR) of 19 761 to 26 391 kg yr^{-1}, compared with TRI emissions of 17 658 kg yr^{-1} and NEI emissions of 6035 kg yr^{-1} for elemental mercury and 25 603 kg yr^{-1} counting all mercury emission types.

There are emissions from the southwest, but these are smaller than would expected from the model by at least a factor of 2. A similar situation holds for the northwest and for the regional sources, with model results about 3 times higher than the TRI. The values for the northeast cannot be compared directly, as they do not include the emissions from Canada. Finally, the local emissions estimated by the model are a factor of 4 higher than the TRI, and a factor of 5 higher than the total mercury emissions from the NEI.

Part of the discrepancy maybe due to the fact that the inventories only include point sources for mercury. Had it been possible, including area sources could reduce the difference with the inverse model results. On the other hand, the synthetic test revealed that in the case of a simple source, the model tended to overestimate total emissions even though it identified the location of the source accurately. It is therefore reasonable to place greater confidence in the spatial pattern and relative magnitude of the emissions than in the absolute emission totals. Nevertheless, on balance the analysis does suggest that the emissions inventories underestimate elemental mercury emissions from sources other than the large coal-fired power plants.

4.2 Time scale analysis

Table 5 above showed that 6 % of GEM was unaccounted for by the model. In order to identify what this might be due to, we perform a time scale analysis as described by Hogrefe et al. (2003) and Hogrefe et al. (2001). We use the Kolmogorov-Zurbenko filter to separate the time series according to the temporal scale of the signal. The concentrations are split into intra-day, diurnal, synoptic and seasonal components. Note that for simplicity, we use the same coefficients as Hogrefe et al. (2003), although that means that our categories include longer timescales because we have data on alternate hours rather than every hour. The contribution of each temporal component to the full time series is obtained by calculating the variance of each component as a fraction of the sum of the variances of all the components.

Table 6 shows the results for the measurement time series, the inverted time series and the residual. This shows clearly that the measurements have components that vary across the whole range of times scales with roughly similar contributions from each category. In contrast, the inverted time series is much lower on the intra-day component, which accounts for 7 % instead of 29 % of the variance. Correspondingly, the synoptic scale accounts for a greater fraction of the variance (43 % instead of 24 %). For the residual, the components are highest in the intra-day scale and lowest in the seasonal scale.

This demonstrates that the inverse model is missing some of the high frequency components of the timeseries. These are due to short spikes in concentrations, which are most likely to be local sources where the plume has not had as much time to dilute. This suggests that the method is more likely to underestimate sources that are close by. Consequently, it can be inferred that a significant fraction of the unaccounted mercury is due to local sources.

4.3 Emission types

The results of this analysis suggest that the emissions of GEM from the lake surfaces are two times higher than those calculated in Sect. 2.4. As noted above, there is considerable spread in the measured concentrations of dissolved gaseous mercury. The inverse model suggests that average values may be towards the higher end of the reported range, well above the 30 $\mathrm{pg\,l^{-1}}$ used in the calculations. This would suggest average fluxes in the range of 4 to 5 $\mathrm{ng\,m^{-2}\,h^{-1}}$ and total emissions from the Great Lakes of 12 000 to 14 000 kg of GEM for the time period of the study.

Forest fires were found to have a clearly detectable signal in the GEM time series, with total impacts around 30 % higher than the lake surface impacts. Most of these are due to emissions in the east domain which includes a large part of the midwest, the northeast and Southeastern Canada. The inverse model suggests that emissions from this area could be underestimated by a factor of 3 to 4. The model further suggests that emissions in the north central domain could be underestimated by a factor of 2 to 3, but that estimates of the emissions form the south central and southeast domains are of the correct magnitude. The domains further away were found to have nil or variable impacts. This could be because there is not enough data in the inversion, either because those areas do not influence the measurement site often enough, or because the level of the impacts is too low relative to other sources. Finally, the FINN model estimated releases of 1383kg of mercury in WRF domain 2, close to the measurement site. The inverse model did not identify any impacts from these. This could be because local sources have short, sharp peaks which can easily suffer from mismatches between the model and the measurements or because the diurnal distribution of the emissions is more important for local sources. As with the gridded emissions, the inverse model does a better job of identifying sources that are further away than near-field ones.

There was one large episode of elevated GEM concentrations starting on 12 November 2004 and lasting until the end of the month which is not accounted for in the inversion, see Fig. 10. Levels rose rapidly to between 4 and 6 ng m^{-3} and decayed slowly over the next 2 weeks. This suggests a large regional source, but the event is puzzling because it lasted over a variety of wind patterns with shifting air masses from both the north and the south. Volcanoes can emit large amounts of mercury during explosions (Bagnato et al., 2011) and could be a possible source. Mount St. Helens in Washington State had renewed eruptions between September 2004 and December 2005 and could possibly be a factor in this event (Sherrod et al., 2008). We simulated forward emissions from the volcano using CAMx in combination with the large WRF domain used for forest fires. Although this source cannot be ruled out, the results did not provide strong evidence in support of this hypothesis.

Grímsvötn in Iceland had a week long eruption starting on 1 November 2004 (Thordarson and Larsen, 2007). We performed forward particle simulations using FLEXPART based on wind fields from the Global Forecast System. Although the arrival time matched the episode in the time series, the simulated concentrations lasted much longer than the measured episode itself. It would therefore seem that such a distant source cannot be responsible for such a clearly defined event. Nevertheless, further analysis of this event may be warranted especially if it can be expanded with concurrent measurements from different sites.

5 Conclusions

This paper developed a hybrid inversion scheme based on particle back-trajectories and forward grid modeling to evaluate sources of elemental mercury using atmospheric measurements in Milwaukee. The method provided estimates of source strengths as well as source impacts at the measurement site. Using bootstrapping, the method further provided confidence intervals on the results.

Identifying local point sources is a particular challenge. The analysis therefore required a combination of analysis methods including meteorological analysis, concentration field analysis and time scale analysis to supplement the inverse method.

In agreement with past studies, it was found that mercury levels are impacted by sources at multiple scales, from small local sources to large distant point sources. The inverted strengths of the coal-fired power plants was in good agreement with current inventories, but other sources seem to be under-represented. These may include waste disposal and incineration as well as metal processing.

The impacts of emissions from the lake surface and from forest fires could be clearly seen in the model inversion. These suggest that emissions from both of these sources are larger than predicted by current emissions models and that they are a significant source of elemental gaseous mercury.

As the inversion uses a hybrid model, it is straightforward to simulate candidate sources using a grid model and include them in the analysis. Soil and vegetation sources could be included in the same way as the lake surface sources. Further examples would depend on the location of the measurement site and could include testing the possibility of emissions from melting snow or the magnitude of emissions from gold mining and underground coal fires.

Acknowledgements. This manuscript was made possible by EPA grant number RD-83455701. Its contents are solely the responsibility of the grantee and do not necessarily represent the official views of the EPA. Further, the EPA does not endorse the purchase of any commercial products or services mentioned in the publication. The initial mercury measurements were funded by US EPA STAR Grant # R829798. We are also grateful to the US EPA for making the National Emissions Inventory and Toxic Release Inventory available, and to the US National Climatic Data Center for the meteorological data.

References

Akagi, S. K., Yokelson, R. J., Wiedinmyer, C., Alvarado, M. J., Reid, J. S., Karl, T., Crounse, J. D., and Wennberg, P. O.: Emission factors for open and domestic biomass burning for use in atmospheric models, Atmos. Chem. Phys., 11, 4039–4072, doi:10.5194/acp-11-4039-2011, 2011. 12945

Ashbaugh, L. L., Malm, W. C., and Sadeh, W. Z.: A residence time probability analysis of sulfur concentrations at Grand-Canyon-National-Park, Atmos. Environ., 19, 1263–1270, 1985. 12942

Bagnato, E., Aiuppa, A., Parello, F., Allard, P., Shinohara, H., Liuzzo, M., and Giudice, G.: New clues on the contribution of Earth's volcanism to the global mercury cycle, B. Volcanol., 73, 497–510, doi:10.1007/s00445-010-0419-y, 2011. 12957

Bash, J. O.: Description and initial simulation of a dynamic bidirectional air-surface exchange model for mercury in Community Multiscale Air Quality (CMAQ) model, J. Geophys. Res.-Atmos., 115, D06305, doi:10.1029/2009JD012834, 2010. 12938

Bash, J. O. and Miller, D. R.: A relaxed eddy accumulation system for measuring surface fluxes of total gaseous mercury, J. Atmos. Ocean. Tech., 25, 244–257, doi:10.1175/2007JTECHA908.1, 2008. 12938

Bash, J., Miller, D., Meyer, T., and Bresnahan, P.: Northeast United States and Southeast Canada natural mercury emissions estimated with a surface emission model, Atmos. Environ., 38, 5683–5692, doi:10.1016/j.atmosenv.2004.05.058, 2004. 12937

Brioude, J., Kim, S.-W., Angevine, W. M., Frost, G. J., Lee, S.-H., McKeen, S. A., Trainer, M., Fehsenfeld, F. C., Holloway, J. S., Ryerson, T. B., Williams, E. J., Petron, G., and Fast, J. D.: Top-down estimate of anthropogenic emission inventories and their interannual variability in Houston using a mesoscale inverse modeling technique, J. Geophys. Res.-Atmos., 116, D20305, doi:10.1029/2011JD016215, 2011. 12945, 12947

Bullock, Jr., O. R., Atkinson, D., Braverman, T., Civerolo, K., Dastoor, A., Davignon, D., Ku, J.-Y., Lohman, K., Myers, T. C., Park, R. J., Seigneur, C., Selin, N. E., Sistla, G., and Vijayaraghavan, K.: The North American Mercury Model Intercomparison Study (NAMMIS): study description and model-to-model comparisons, J. Geophys. Res.-Atmos., 113, D17310, doi:10.1029/2008JD009803, 2008. 12938

Carroll, M., Townshend, J., Hansen, M., DiMiceli, C., Sohlberg, R., and Wurster, K.: Vegetative cover conversion and vegetation continuous fields, in: Land Remote Sensing and Global Environmental Change: NASA's Earth Observing System and the Science of Aster and MODIS, edited by: Ramachandran, B., Justice, C. O., and Abrams, M., Springer-Verlag, Chapter 32, 725–745, Springer-Verlag, New York, USA, doi:10.1007/978-1-4419-6749-7, 2011. 12945

Cheng, I., Lu, J., and Song, X.: Studies of potential sources that contributed to atmospheric mercury in Toronto, Canada, Atmos. Environ., 43, 6145–6158, doi:10.1016/j.atmosenv.2009.09.008, 2009. 12940

Cheng, I., Zhang, L., Blanchard, P., Graydon, J. A., and St. Louis, V. L.: Source-receptor relationships for speciated atmospheric mercury at the remote Experimental Lakes Area, northwestern Ontario, Canada, Atmos. Chem. Phys., 12, 1903–1922, doi:10.5194/acp-12-1903-2012, 2012. 12940

Ci, Z., Zhang, X., and Wang, Z.: Elemental mercury in coastal seawater of Yellow Sea, China: temporal variation and air-sea exchange, Atmos. Environ., 45, 183–190, doi:10.1016/j.atmosenv.2010.09.025, 2011a. 12943

Ci, Z. J., Zhang, X. S., Wang, Z. W., Niu, Z. C., Diao, X. Y., and Wang, S. W.: Distribution and air-sea exchange of mercury (Hg) in the Yellow Sea, Atmos. Chem. Phys., 11, 2881–2892, doi:10.5194/acp-11-2881-2011, 2011b. 12943

Cohen, M., Artz, R., Draxler, R., Miller, P., Poissant, L., Niemi, D., Ratte, D., Deslauriers, M., Duval, R., Laurin, R., Slotnick, J., Nettesheim, T., and McDonald, J.: Modeling the atmospheric transport and deposition of mercury to the Great Lakes, Environ. Res., 95, 247–265, doi:10.1016/j.envres.2003.11.007, 2004. 12939

Doran, J. C., Fast, J. D., Barnard, J. C., Laskin, A., Desyaterik, Y., and Gilles, M. K.: Applications of lagrangian dispersion modeling to the analysis of changes in the specific absorption of elemental carbon, Atmos. Chem. Phys., 8, 1377–1389, doi:10.5194/acp-8-1377-2008, 2008. 12942

Engle, M. A., Tate, M. T., Krabbenhoft, D. P., Schauer, J. J., Kolker, A., Shanley, J. B., and Bothner, M. H.: Comparison of atmospheric mercury speciation and deposition at nine sites across Central and Eastern North America, J. Geophys. Res.-Atmos., 115, D18306, doi:10.1029/2010JD014064, 2010. 12938, 12939

Enting, I. G.: Inverse Problems in Atmospheric Constituent Transport, Cambridge University Press, Cambridge University Press, Cambridge, UK, 2002. 12945

ENVIRON: CAMx, comprehensive air quality model with extensions, User's Guide, Tech. Rep. Version 5.40, ENVIRON International Corporation, ENVIRON International Corporation, Novato, California, USA, 2011. 12944

Fast, J. D. and Easter, R.: A Lagrangian particle dispersion model compatible with WRF, in: 7th WRF User's Workshop, Boulder, CO, 19–22 June 2006, Abstract P6.2, 2006. 12942

de Foy, B., Lei, W., Zavala, M., Volkamer, R., Samuelsson, J., Mellqvist, J., Galle, B., Martínez, A.-P., Grutter, M., Retama, A., and Molina, L. T.: Modelling constraints on the emission inventory and on vertical dispersion for CO and SO_2 in the Mexico City Metropolitan Area using Solar FTIR and zenith sky UV spectroscopy, Atmos. Chem. Phys., 7, 781–801, doi:10.5194/acp-7-781-2007, 2007. 12942

de Foy, B., Zavala, M., Bei, N., and Molina, L. T.: Evaluation of WRF mesoscale simulations and particle trajectory analysis for the MILAGRO field campaign, Atmos. Chem. Phys., 9, 4419–4438, doi:10.5194/acp-9-4419-2009, 2009. 12942

de Foy, B., Smyth, A. M., Thompson, S. L., Gross, D. S., Olson, M. R., Sager, N., and Schauer, J. J.: Sources of nickel, vanadium and black carbon in aerosols in Milwaukee, Atmos. Environ., submitted, 2012. 12941

Friedl, M. A., Sulla-Menashe, D., Tan, B., Schneider, A., Ramankutty, N., Sibley, A., and Huang, X.: MODIS collection 5 global land cover: algorithm refinements and characterization of new datasets, Remote Sens. Environ., 114, 168–182, doi:10.1016/j.rse.2009.08.016, 2010. 12944

Gbor, P., Wen, D., Meng, F., Yang, F., Zhang, B., and Sloan, J.: Improved model for mercury emission, transport and deposition, Atmos. Environ., 40, 973–983, doi:10.1016/j.atmosenv.2005.10.040, 2006. 12938

Gbor, P. K., Wen, D., Meng, F., Yang, F., and Sloan, J. J.: Modeling of mercury emission, transport and deposition in North America, Atmos. Environ., 41, 1135–1149, doi:10.1016/j.atmosenv.2006.10.005, 2007. 12938

Giglio, L., Descloitres, J., Justice, C., and Kaufman, Y.: An enhanced contextual fire detection algorithm for MODIS, Remote Sens. Environ., 87, 273–282, doi:10.1016/S0034-4257(03)00184-6, 2003. 12944

Han, Y., Holsen, T., Hopke, P., and Yi, S.: Comparison between back-trajectory based modeling and Lagrangian backward dispersion modeling for locating sources of reactive gaseous mercury, Environ. Sci. Technol., 39, 1715–1723, doi:10.1021/es0498540, 2005. 12940

Han, Y.-J., Holsen, T. M., and Hopke, P. K.: Estimation of source locations of total gaseous mercury measured in New York State using trajectory-based models, Atmos. Environ., 41, 6033–6047, doi:10.1016/j.atmosenv.2007.03.027, 2007. 12940

Hansen, M., Townshend, J., Defries, R., and Carroll, M.: Estimation of tree cover using MODIS data at global, continental and regional/local scales, Int. J. Remote Sens., 26, 4359–4380, 2005. 12945

Hansen, M. C., DeFries, R. S., Townshend, J. R. G., Carroll, M., Dimiceli, C., and Sohlberg, R. A.: Global percent tree cover at a spatial resolution of 500 meters: first results of the MODIS vegetation continuous fields algorithm, Earth Interact., 7, 1–15, doi:10.1175/1087-3562(2003)007<0001:GPTCAA>2.0.CO;2 2003. 12945

Henze, D. K., Seinfeld, J. H., and Shindell, D. T.: Inverse modeling and mapping US air quality influences of inorganic $PM_{2.5}$ precursor emissions using the adjoint of GEOS-Chem, Atmos. Chem. Phys., 9, 5877–5903, doi:10.5194/acp-9-5877-2009, 2009. 12947

Hoelzemann, J., Schultz, M., Brasseur, G., Granier, C., and Simon, M.: Global wildland fire emission model (GWEM): evaluating the use of global area burnt satellite data, J. Geophys. Res.-Atmos., 109, D14S04, doi:10.1029/2003JD003666, 2004. 12945

Hogrefe, C., Rao, S., Kasibhatla, P., Hao, W., Sistla, G., Mathur, R., and McHenry, J.: Evaluating the performance of regional-scale photochemical modeling systems: Part II – ozone predictions, Atmos. Environ., 35, 4175–4188, doi:10.1016/S1352-2310(01)00183-2, 2001. 12955

Hogrefe, C., Vempaty, S., Rao, S., and Porter, P.: A comparison of four techniques for separating different time scales in atmospheric variables, Atmos. Environ., 37, 313–325, doi:10.1016/S1352-2310(02)00897-X, 2003. 12955

Hong, S. Y., Noh, Y., and Dudhia, J.: A new vertical diffusion package with an explicit treatment of entrainment processes, Mon. Weather Rev., 134, 2318–2341, 2006. 12942

Huang, J., Choi, H.-D., Hopke, P. K., and Holsen, T. M.: Ambient mercury sources in Rochester, NY: results from principle components analysis (PCA) of mercury monitoring network data, Environ. Sci. Technol., 44, 8441–8445, doi:10.1021/es102744j, 2010. 12940

Kain, J. S.: The Kain–Fritsch convective parameterization: an update, J. Appl. Meteorol., 43, 170–181, 2004. 12942

Kolker, A., Olson, M. L., Krabbenhoft, D. P., Tate, M. T., and Engle, M. A.: Patterns of mercury dispersion from local and regional emission sources, rural Central Wisconsin, USA, Atmos. Chem. Phys., 10, 4467–4476, doi:10.5194/acp-10-4467-2010, 2010. 12939

Kuss, J., Holzmann, J., and Ludwig, R.: An elemental mercury diffusion coefficient for natural waters determined by molecular dynamics simulation, Environ. Sci. Technol., 43, 3183–3186, doi:10.1021/es8034889, 2009. 12943

Lai, S.-O., Holsen, T. M., Han, Y.-J., Hopke, P. P., Yi, S.-M., Blanchard, P., Pagano, J. J., and Milligan, M.: Estimation of mercury loadings to Lake Ontario: results from the Lake Ontario atmospheric deposition study (LOADS), Atmos. Environ., 41, 8205–8218, doi:10.1016/j.atmosenv.2007.06.035, 2007. 12943

Lauvaux, T., Uliasz, M., Sarrat, C., Chevallier, F., Bousquet, P., Lac, C., Davis, K. J., Ciais, P., Denning, A. S., and Rayner, P. J.: Mesoscale inversion: first results from the CERES campaign with synthetic data, Atmos. Chem. Phys., 8, 3459–3471, doi:10.5194/acp-8-3459-2008, 2008. 12945

Lin, C., Lindberg, S., Ho, T., and Jang, C.: Development of a processor in BEIS3 for estimating vegetative mercury emission in the continental United States, 7th International Conference on Mercury as a Global Pollutant, Ljubljana, Slovenia, 28 June–2 July 2004, Atmos. Environ., 39, 7529–7540, doi:10.1016/j.atmosenv.2005.04.044, 2005. 12937

Lin, X. and Tao, Y.: A numerical modelling study on regional mercury budget for Eastern North America, Atmos. Chem. Phys., 3, 535–548, doi:10.5194/acp-3-535-2003, 2003. 12938

Lindberg, S., Bullock, R., Ebinghaus, R., Engstrom, D., Feng, X., Fitzgerald, W., Pirrone, N., Prestbo, E., and Seigneur, C.: A synthesis of progress and uncertainties in attributing the sources of mercury in deposition, 8th International Conference on Mercury as a Global Pollutant, Madison, WI, 6–11 August 2006, Ambio, 36, 19–32, 2007. 12936, 12937

Liu, B., Keeler, G. J., Dvonch, J. T., Barres, J. A., Lynam, M. M., Marsik, F. J., and Morgan, J. T.: Urban-rural differences in atmospheric mercury speciation, Atmos. Environ., 44, 2013–2023, doi:10.1016/j.atmosenv.2010.02.012, 2010. 12940

Manolopoulos, H., Schauer, J. J., Purcell, M. D., Rudolph, T. M., Olson, M. L., Rodger, B., and Krabbenhoft, D. P.: Local and regional factors affecting atmospheric mercury speciation at a remote location, J. Environ. Eng. Sci., 6, 491–501, doi:10.1139/S07-005, 2007a. 12939, 12940

Manolopoulos, H., Snyder, D. C., Schauer, J. J., Hill, J. S., Turner, J. R., Olson, M. L., and Krabbenhoft, D. P.: Sources of speciated atmospheric mercury at a residential neighborhood impacted by industrial sources, Environ. Sci. Technol., 41, 5626–5633, doi:10.1021/es0700348, 2007b. 12940

Mergler, D., Anderson, H. A., Chan, L. H. M., Mahaffey, K. R., Murray, M., Sakamoto, M., and Stern, A. H.: Methylmercury exposure and health effects in humans: a worldwide concern, 8th International Conference on Mercury as a Global Pollutant, Madison, WI, 6–11 August 2006, Ambio, 36, 3–11, 2007. 12936

Mesinger, F., DiMego, G., Kalnay, E., Mitchell, K., Shafran, P., Ebisuzaki, W., Jovic, D., Woollen, J., Rogers, E., Berbery, E., Ek, M., Fan, Y., Grumbine, R., Higgins, W., Li, H., Lin, Y., Manikin, G., Parrish, D., and Shi, W.: North American regional reanalysis, B. Am. Meteorol. Soc., 87, 343, doi:10.1175/BAMS-87-3-343, 2006. 12941

Murray, M. and Holmes, S.: Assessment of mercury emissions inventories for the Great Lakes states, Workshop on an Ecosystem Approach to the Health Effects of Mercury in the Great Lakes Basin, Windsor, CANADA, 26–27 February 2003, Environ. Res., 95, 282–297, doi:10.1016/j.envres.2004.02.007, 2004. 12939

O'Brien, J. J.: A note on the vertical structure of the eddy exchange coefficient in the planetary boundary layer, J. Atmos. Sci., 27, 1214–1215, 1970. 12944

Pirrone, N., Cinnirella, S., Feng, X., Finkelman, R. B., Friedli, H. R., Leaner, J., Mason, R., Mukherjee, A. B., Stracher, G. B., Streets, D. G., and Telmer, K.: Global mercury emissions to the atmosphere from anthropogenic and natural sources, Atmos. Chem. Phys., 10, 5951–5964, doi:10.5194/acp-10-5951-2010, 2010. 12937

Poissant, L., Amyot, M., Pilote, M., and Lean, D.: Mercury water-air exchange over the Upper St. Lawrence River and Lake Ontario, Environ. Sci. Technol., 34, 3069–3078, doi:10.1021/es990719a, 2000. 12943

Rigby, M., Manning, A. J., and Prinn, R. G.: Inversion of long-lived trace gas emissions using combined Eulerian and Lagrangian chemical transport models, Atmos. Chem. Phys., 11, 9887–9898, doi:10.5194/acp-11-9887-2011, 2011. 12945, 12946

Roustan, Y. and Bocquet, M.: Inverse modelling for mercury over Europe, Atmos. Chem. Phys., 6, 3085–3098, doi:10.5194/acp-6-3085-2006, 2006. 12938

Rutter, A. P., Schauer, J. J., Lough, G. C., Snyder, D. C., Kolb, C. J., Von Klooster, S., Rudolf, T., Manolopoulos, H., and Olson, M. L.: A comparison of speciated atmospheric mercury at an urban center and an upwind rural location, J. Environ. Monitor., 10, 102–108, doi:10.1039/b710247j, 2008. 12939, 12940, 12941, 12943, 12948, 12949, 12952

Schroeder, W. and Munthe, J.: Atmospheric mercury – an overview, 4th International Conference on Mercury as a Global Pollutant, Hamburg, Germany, 4–8 August 1996, Atmos. Environ., 32, 809–822, doi:10.1016/S1352-2310(97)00293-8, 1998. 12936, 12937

Seibert, P., Kromp-Kolb, H., Baltensperger, U., Jost, D. T., and Schwikowski, M.: Trajectory analysis of high-alpine air pollution data, in: Air Pollution Modelling and its Application X, edited by: Gryning, S.-E. and Millan, M. M., Plenum Press, New York, 595–596, 1994. 12942

Seigneur, C.: Estimating the Contribution of Coal-Fired Power Plants to the Atmospheric Deposition of Mercury in Wisconsin, Tech. Rep. CP263-1a, Atmospheric and Environmental Research, Inc., San Ramon, California, USA, 2007. 12938

Seigneur, C., Vijayaraghavan, K., Lohman, K., Karamchandani, P., and Scott, C.: Global source attribution for mercury deposition in the United States, Environ. Sci. Technol., 38, 555–569, doi:10.1021/es034109t, 2004. 12938

Selin, N. E.: Global biogeochemical cycling of mercury: a review, Annu. Rev. Env. Resour., 34, 43–63, doi:10.1146/annurev.environ.051308.084314, 2009. 12936

Sherrod, D. R., Scott, W. E., and Stauffer, P. H.: A Volcano Rekindled: the Renewed Eruption of Mount St. Helens, 2004–2006, Tech. rep., US Geological Survey, available at: http://pubs.er.usgs.gov/publication/pp1750, last access: 21 May 2012, 2008. 12957

Sigler, J. M., Mao, H., and Talbot, R.: Gaseous elemental and reactive mercury in Southern New Hampshire, Atmos. Chem. Phys., 9, 1929–1942, doi:10.5194/acp-9-1929-2009, 2009. 12938

Skamarock, W. C., Klemp, J. B., Dudhia, J., Gill, D. O., Barker, D. M., Wang, W., and Powers, J. G.: A Description of the Advanced Research WRF Version 2, Tech. Rep. NCAR/TN-468+STR, NCAR, Boulder, Colorado, USA, 2005. 12941

Slemr, F., Brunke, E.-G., Ebinghaus, R., and Kuss, J.: Worldwide trend of atmospheric mercury since 1995, Atmos. Chem. Phys., 11, 4779–4787, doi:10.5194/acp-11-4779-2011, 2011. 12937

Soerensen, A. L., Sunderland, E. M., Holmes, C. D., Jacob, D. J., Yantosca, R. M., Skov, H., Christensen, J. H., Strode, S. A., and Mason, R. P.: An improved global model for air-sea exchange of mercury: high concentrations over the North Atlantic, Environ. Sci. Technol., 44, 8574–8580, doi:10.1021/es102032g, 2010. 12938

Sprovieri, F., Pirrone, N., Ebinghaus, R., Kock, H., and Dommergue, A.: A review of worldwide atmospheric mercury measurements, Atmos. Chem. Phys., 10, 8245–8265, doi:10.5194/acp-10-8245-2010, 2010. 12938

Stohl, A., Forster, C., Frank, A., Seibert, P., and Wotawa, G.: Technical note: The Lagrangian particle dispersion model FLEXPART version 6.2, Atmos. Chem. Phys., 5, 2461–2474, doi:10.5194/acp-5-2461-2005, 2005. 12942

Stohl, A., Seibert, P., Arduini, J., Eckhardt, S., Fraser, P., Greally, B. R., Lunder, C., Maione, M., Mühle, J., O'Doherty, S., Prinn, R. G., Reimann, S., Saito, T., Schmidbauer, N., Simmonds, P. G., Vollmer, M. K., Weiss, R. F., and Yokouchi, Y.: An analytical inversion method for determining regional and global emissions of greenhouse gases: Sensitivity studies and application to halocarbons, Atmos. Chem. Phys., 9, 1597–1620, doi:10.5194/acp-9-1597-2009, 2009. 12945, 12947

Streets, D. G., Devane, M. K., Lu, Z., Bond, T. C., Sunderland, E. M., and Jacob, D. J.: All-time releases of mercury to the atmosphere from human activities, Environ. Sci. Technol., 45, 10485–10491, doi:10.1021/es202765m, 2011. 12937

Tarantola, A.: Inverse Problem Theory, Methods for Data Fitting and Model Parameter Estimation, Elsevier, The Netherlands, 1987. 12945

Thordarson, T. and Larsen, G.: Volcanism in Iceland in historical time: volcano types, eruption styles and eruptive history, J. Geodyn., 43, 118–152, doi:10.1016/j.jog.2006.09.005, 2007. 12957

Vette, A., Landis, M., and Keeler, G.: Deposition and emission of gaseous mercury to and from Lake Michigan during the Lake Michigan Mass Balance Study (July 1994, October 1995), Environ. Sci. Technol., 36, 4525–4532, doi:10.1021/es0112184, 2002. 12943

Wanninkhof, R.: Relationship between wind speed and gas exchange over the ocean, J. Geophys. Res.-Atmos., 97, 7373–7382, 1992. 12943

Wen, D., Lin, J. C., Meng, F., Gbor, P. K., He, Z., and Sloan, J. J.: Quantitative assessment of upstream source influences on total gaseous mercury observations in Ontario, Canada, Atmos. Chem. Phys., 11, 1405–1415, doi:10.5194/acp-11-1405-2011, 2011. 12940

Wiedinmyer, C. and Friedli, H.: Mercury emission estimates from fires: an initial inventory for the United States, Environ. Sci. Technol., 41, 8092–8098, doi:10.1021/es071289o, 2007. 12945

Wiedinmyer, C., Quayle, B., Geron, C., Belote, A., McKenzie, D., Zhang, X., O'Neill, S., and Wynne, K. K.: Estimating emissions from fires in North America for air quality modeling, Atmos. Environ., 40, 3419–3432, doi:10.1016/j.atmosenv.2006.02.010, 2006. 12944

Wiedinmyer, C., Akagi, S. K., Yokelson, R. J., Emmons, L. K., Al-Saadi, J. A., Orlando, J. J., and Soja, A. J.: The Fire INventory from NCAR (FINN): a high resolution global model to estimate the emissions from open burning, Geosci. Model Dev., 4, 625–641, doi:10.5194/gmd-4-625-2011, 2011. 12944

Yarwood, G., Lau, S., Jia, Y., Karamchandani, P., and Vijayaraghavan, K.: Modeling Atmospheric Mercury Chemistry and Deposition with CAMx for a 2002 Annual Simulations, Tech. rep., ENVIRON International Corporation, Novato, California, CA, USA, 2003. 12938

Table 1. Total emissions from lake surface emissions for the 318 days of the measurements for the domains shown in Fig. 2.

Lake	Emissions (kg)	Average flux ($\mathrm{ng\,m^{-2}\,h^{-1}}$)
Michigan	1698	2.7
Superior	2396	2.6
Huron	1687	2.1
Erie	657	2.3
Ontario	412	2.0
Total	6849	2.3

Table 2. Total emissions of GEM from forest fires for the 318 days of the measurements for the domains shown in Fig. 3.

Domain	Emissions (kg)
WRF D2	1383
East	7521
Southeast	43 305
South central	15 987
North central	7157
West	8914
Pacific Northwest	46 329
Northern Canada	76 903
Alaska	85 116
Total	292 595

Table 3. Gridded emission totals for domains shown in Fig. 11.

Emissions (kg yr^{-1})	Median	Lower-quartile	Upper-quartile	TRI 2004	GEM NEI 2002	Hg NEI 2002
Local (50 km radius)	984	835	1164	217	71	193
South regional	6071	5023	7503	1887	1551	3248
Northeast	13 198	10 569	17 194	1510	578	2276
Southeast	23 003	19 761	26 391	17 658	6035	25 603
West regional	3523	2662	4922	1158	251	1430
Southwest	23 770	20 942	27 367	7163	3796	9701
Northwest	5761	4331	7346	1582	832	3480
Total	76 310	64 123	91 887	31 176	13 114	45 932

Table 4. Scaling factors for forest fires emissions and lake surface emissions shown in Fig. 9.

Domain	Median	Lower-quartile	Upper-quartile
WRF D2	0	0	0
East	3.9	3.1	4.5
Southeast	1.1	0.6	1.6
South central	1.2	0.8	1.6
North central	2.6	2.2	3.3
West	6.7	3.9	10.1
Pacific northwest	0.0	0.0	0.0
Northern Canada	0.1	0.0	0.2
Alaska	0	0	0
Lake surface	1.9	1.7	2.2

Table 5. Contribution of different source groups to the annual average GEM concentration ($\mathrm{pg\,m^{-3}}$) at the receptor site.

Source group		Median	Lower-quartile	Upper-quartile
Grids	Local (50 km radius)	63.8	54.1	71.7
	South regional	29.7	25.8	35.9
	Northeast	26.6	21.0	33.6
	Southeast	16.2	13.1	19.4
	West regional	15.8	11.5	21.7
	Southwest	22.9	19.0	25.0
	Northwest	10.6	8.2	14.2
Total Grid		187.9	177.3	202.2
Fires	WRF d2	0.0	0.0	0.0
	East	46.2	36.6	52.8
	Southeast	11.6	6.2	16.5
	South central	8.2	5.6	10.7
	North central	10.6	8.8	13.4
	West	5.5	3.2	8.3
	Pacific northwest	0.0	0.0	0.4
	Northern Canada	4.2	0.7	6.3
	Alaska	0.0	0.0	0.0
Total Fires		86.2	61.0	108.3
Lake surface		61.2	53.8	71.5
Local and regional background		490.0	480.0	510.0
Global background		1500.0	1500.0	1500.0
Unaccounted for in model		149.2	144.3	150.4
Inverted timeseries		2330.3	2323.9	2341.1
Measurements		2479.5	2468.2	2491.4

Title Page
Abstract Introduction
Conclusions References
Tables Figures
◀I ▶I
◀ ▶
Back Close
Full Screen / Esc
Printer-friendly Version
Interactive Discussion

Table 6. Time scale analysis of the measurements, the inverted timeseries and the residual. This shows the percent of variance in the timeseries due to components with different time scales. The measurements contains variations at all time scales, but the inverted time series does not account sufficiently for hourly variations.

Time scale	Measurement	Inverted timeseries	Residual
Intra-day	29	7	34
Diurnal	24	23	29
Synoptic	24	43	21
Seasonal	23	27	16

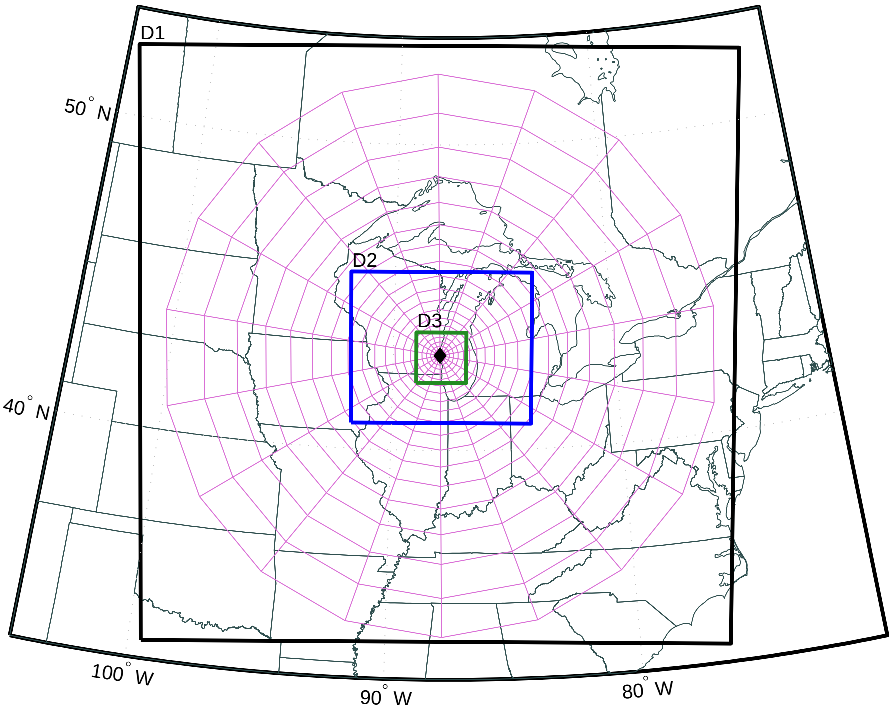

Fig. 1. Map showing the 3 WRF domains (black, blue and green) and the polar grid used for the inverse model (pink) (particle back-trajectories were mapped onto the polar grid for the Residence Time Analysis).

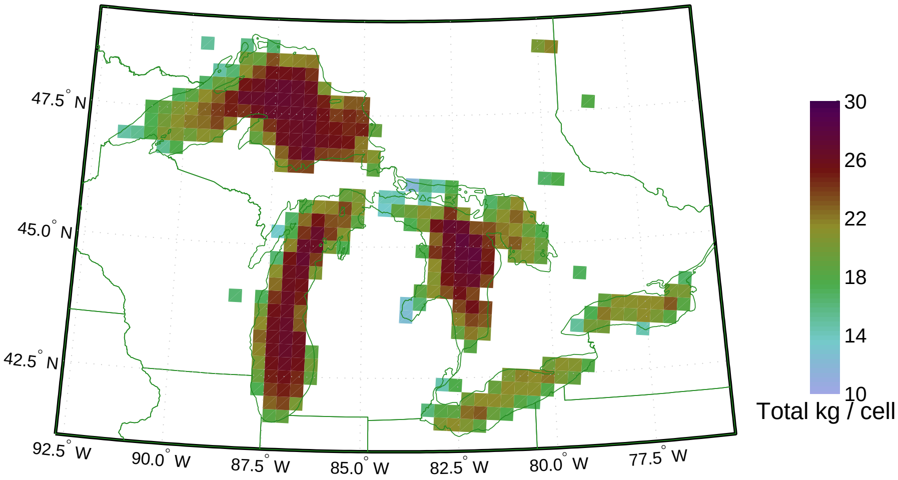

Fig. 2. Gaseous elemental mercury emissions from the lake surfaces summed from 28 June 2004 to 11 May 2005 for WRF domain 1. See Table 1 for total emissions from each lake.

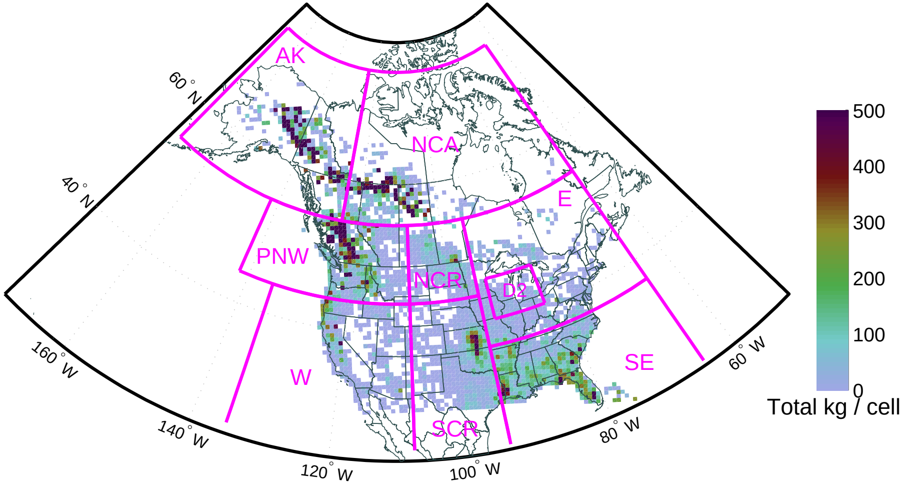

Fig. 3. Forest fires emissions from 28 June 2004 to 11 May 2005, showing the different domains used: Alaska (AK), Northern Canada (NCA), pacific northwest (PNW), west (W), north central (NCR), south central (SCR), east (E), southeast (SE). Note that the east domain does not include WRF domain 2 (D2) which is calculated separately. The maximum emissions in a cell is 7224 kg, in Alaska. See Table 2 for total emissions by domain.

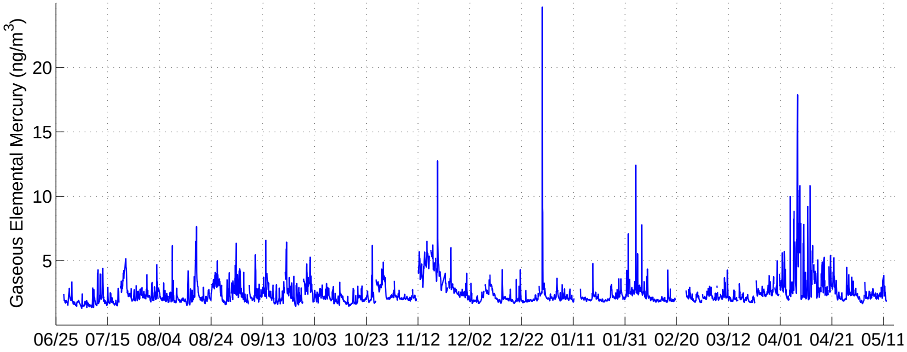

Fig. 4. Time series of elemental gaseous mercury in Milwaukee from 28 June 2004 to 11 May 2005. This shows a combination of variations across time scales from short peaks lasting hours or less to longer events lasting days or even weeks.

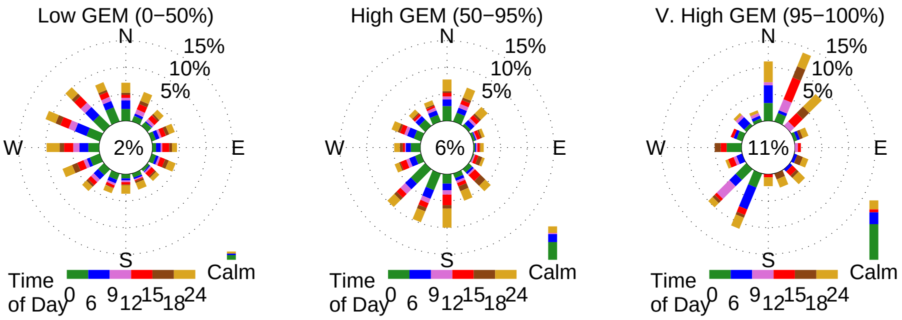

Fig. 5. Wind roses separated according to concentrations of gaseous elemental mercury. Left: 1780 h with concentrations in the bottom 50 %, middle: 1636 h with concentration in the 50 to 95 % interval and right: 179 h with concentrations in the top 5 %. The dominant wind direction for low values is from the northwest, for high values it is from the south/southwest and from the north, and for the highest peaks it is from the northeast and from the southwest. Percentage of hours with calm winds shown in the middle circle.

Title Page
Abstract | Introduction
Conclusions | References
Tables | Figures
◀| |▶
◀ ▶
Back | Close
Full Screen / Esc
Printer-friendly Version
Interactive Discussion

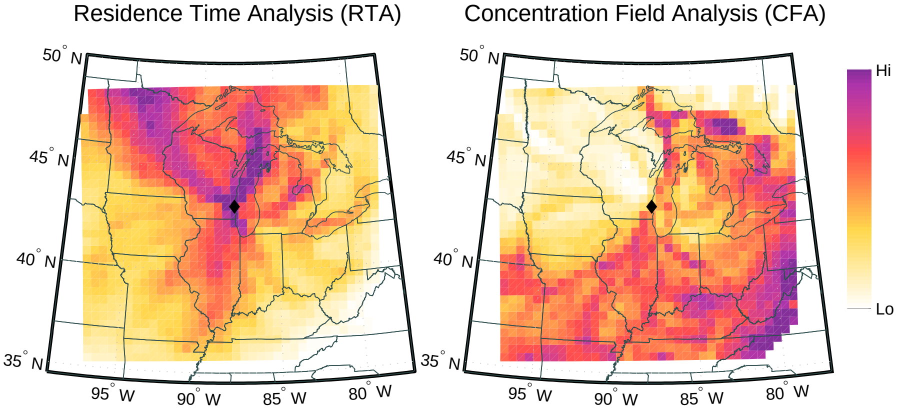

Fig. 6. Residence Time Analysis (RTA, left) and Concentration Field Analysis (CFA, right) for hourly back-trajectories from Milwaukee from 28 June 2004 to 11 May 2005. Measurement site shown by the diamonds. RTA shows dominant surface transport from the northwest, over the lake from the northeast, and from the south through Illinois. CFA shows low potential source regions to the northwest, medium to the south and north and highest towards the Ohio River Valley.

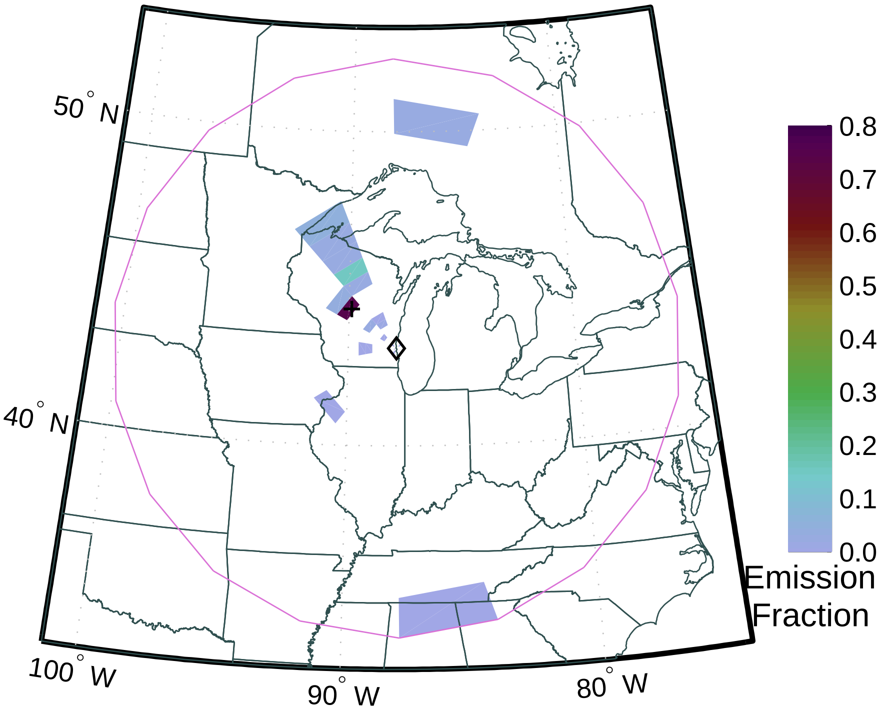

Fig. 7. Map of emissions from the inverse model using synthetic simulations from a location (+) 213 km northwest of the receptor site (diamond). Units are fraction of the synthetic release. Extent of the back-trajectory grid used for the inversion shown in pink.

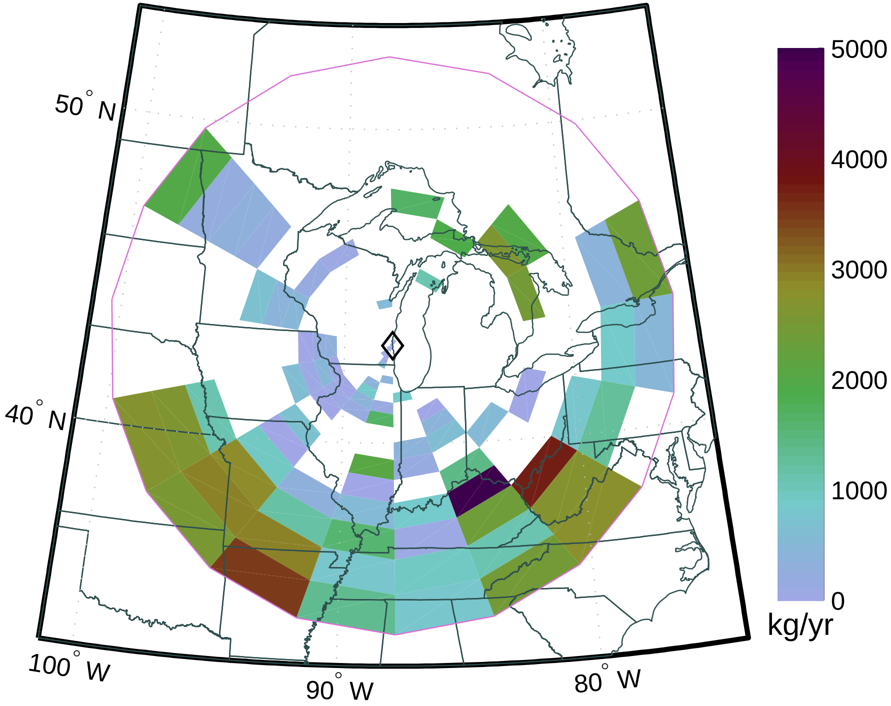

Fig. 8. Map of inverse gridded emissions showing the median of 100 bootstrapped runs. Extent of the back-trajectory grid used for the inversion shown in pink.

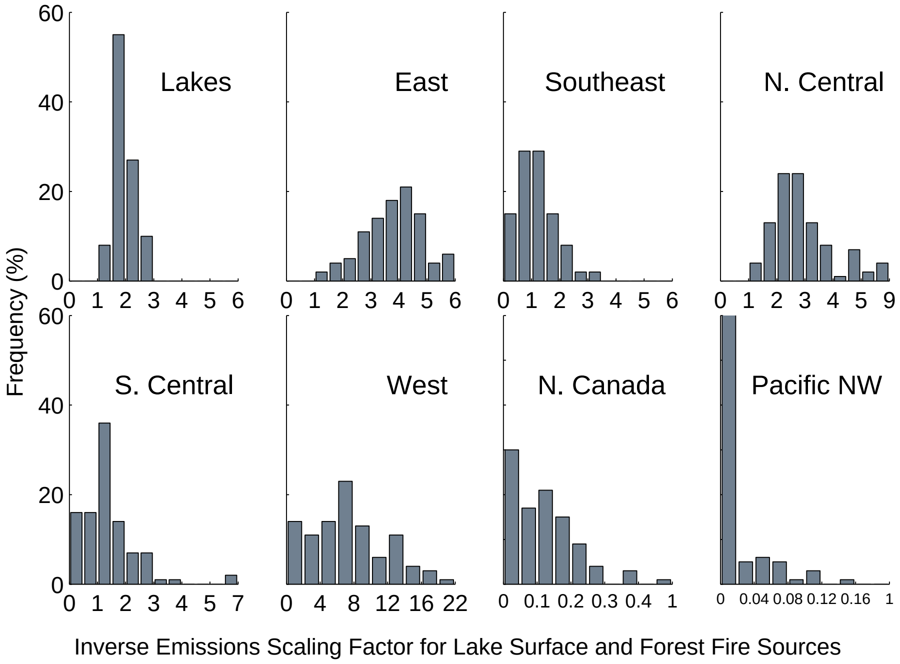

Fig. 9. Histograms of inverse emissions scaling factors for emissions from the Great Lakes and from forest fires by domain. See Fig. 2 for map of lake emissions and Fig. 3 for map of forest fire emissions. (Note that factors for Alaska and WRF D2 are always 0.)

Title Page
Abstract Introduction
Conclusions References
Tables Figures
◀◀ ▶▶
◀ ▶
Back Close
Full Screen / Esc
Printer-friendly Version
Interactive Discussion

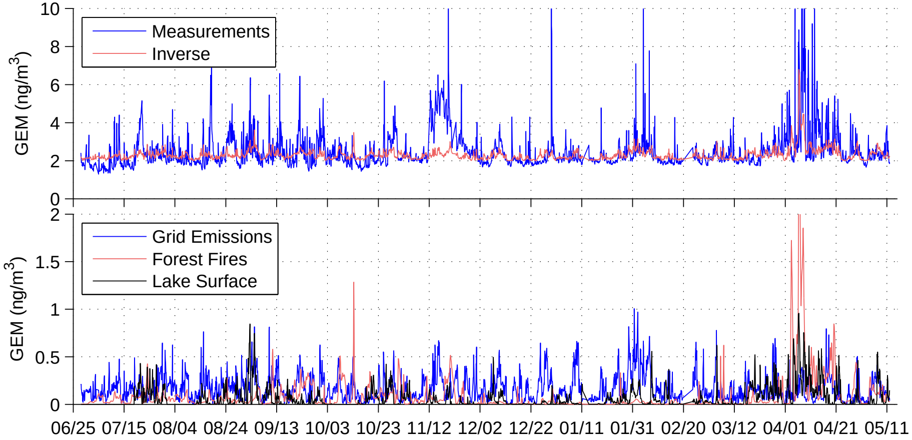

Fig. 10. Original measured and inverse timeseries of GEM (top), with contributions to the inverted timeseries by grid, forest fires and lake surface emissions (bottom), June 2004 to May 2005.

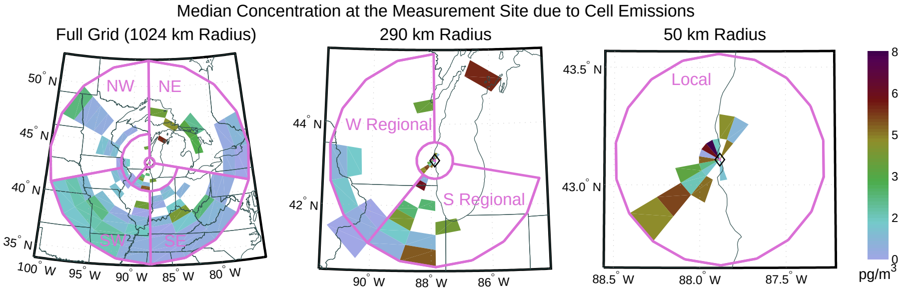

Fig. 11. Map of impacts at the receptor site. Color indicates the average GEM concentration at the measurement site due to emissions in that cell. Domain names and boundaries used in Tables 3 and 5 shown in pink.

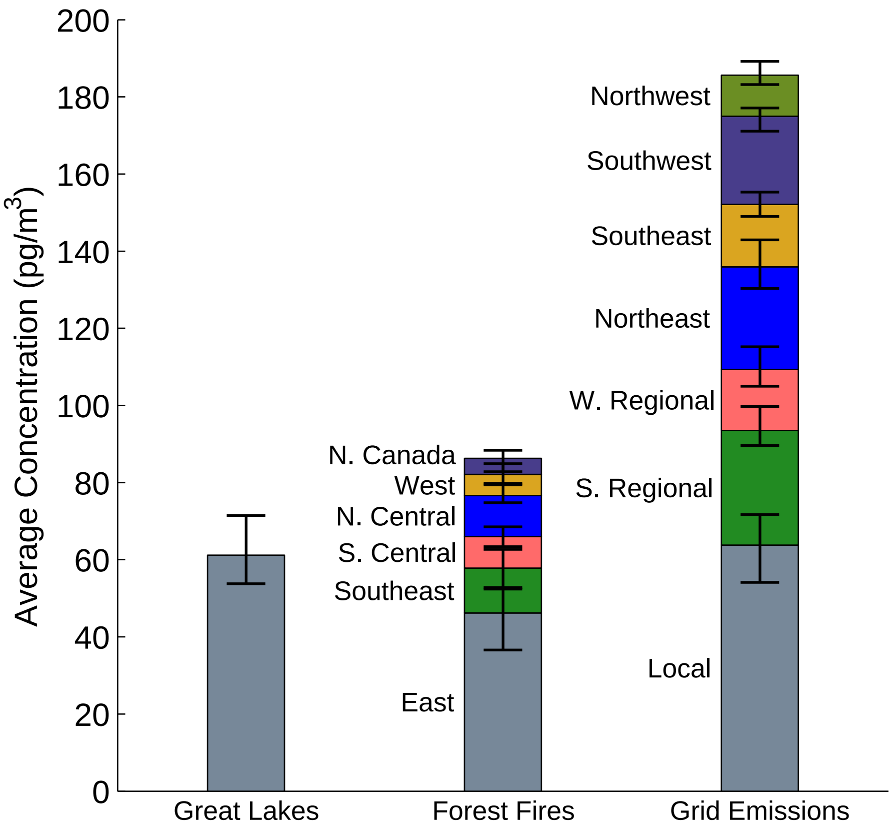

Fig. 12. Impacts from different source groups on the average GEM concentration at the measurement site. Error bars indicate the inter-quartile range of the inverse model estimates from the bootstrapped simulations. See also Table 5.

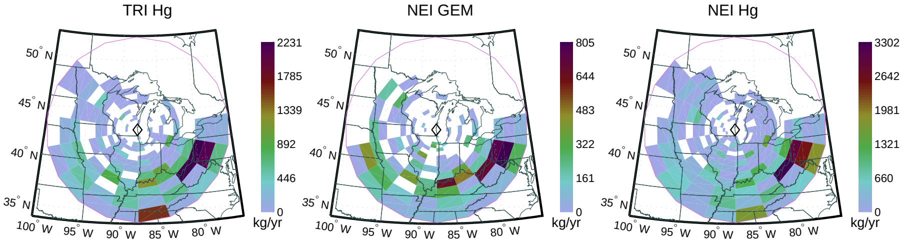

Fig. 13. Map of inventories of all mercury compounds from the Toxic Release Inventory (left), of GEM from the 2002 National Emissions Inventory (middle) and all mercury compounds from the 2002 NEI (right). Extent of the back-trajectory grid used for the inversion shown in pink.